JGR Oceans

RESEARCH ARTICLE
10.1029/2022JC019197

# Winter Vertical Diffusion Rates in the Arctic Ocean, Estimated From $^{7}$Be Measurements and Dissipation Rate Profiles

**K. Schulz[1,2], D. Kadko[3,†], V. Mohrholz[4], M. Stephens[3], and I. Fer[5]**

[1]Oden Institute for Computational Engineering and Sciences, The University of Texas at Austin, Austin, TX, USA, [2]Alfred Wegener Institute Helmholtz Centre for Polar and Marine Research, Physical Oceanography of Polar Seas, Bremerhaven, Germany, [3]Applied Research Center, Florida International University, Miami, FL, USA, [4]Leibniz Institute for Baltic Sea Research, Physical Oceanography and Instrumentation, Rostock, Germany, [5]Geophysical Institute, University of Bergen and Bjerknes Centre for Climate Research, Bergen, Norway

†Deceased 20 February 2022.

**Key Points:**

- Arctic Ocean vertical diffusivity ($K_z$) in the upper halocline in winter is O($10^{-6}$) m$^2$ s$^{-1}$
- Diffusivity estimates from $^{7}$Be measurements and ocean microstructure profiling agree within a factor of 2
- $K_z$ estimates from turbulent dissipation rate profiles are sensitive to the averaging method

**Correspondence to:**

K. Schulz,
kiki.schulz@utexas.edu

**Citation:**

Schulz, K., Kadko, D., Mohrholz, V., Stephens, M., & Fer, I. (2023). Winter vertical diffusion rates in the Arctic Ocean, estimated from $^{7}$Be measurements and dissipation rate profiles. *Journal of Geophysical Research: Oceans*, *128*, e2022JC019197. https://doi.org/10.1029/2022JC019197

Received 12 AUG 2022
Accepted 3 FEB 2023



**Abstract** Ocean turbulent mixing is a key process affecting the uptake and redistribution of heat, carbon, nutrients, oxygen and other dissolved gasses. Vertical turbulent diffusivity sets the rates of water mass transformations and ocean mixing, and is intrinsically an average quantity over process time scales. Estimates based on microstructure profiling, however, are typically obtained as averages over individual profiles. How representative such averaged diffusivities are, remains unexplored in the quiescent Arctic Ocean. Here, we compare upper ocean vertical diffusivities in winter, derived from the $^{7}$Be tracer-based approach to those estimated from direct turbulence measurements during the year-long Multidisciplinary drifting Observatory for the Study of Arctic Climate (MOSAiC) expedition, 2019–2020. We found that diffusivity estimates from both methods agree within their respective measurement uncertainties. Diffusivity estimates obtained from dissipation rate profiles are sensitive to the averaging method applied, and the processing and analysis of similar data sets must take this sensitivity into account. Our findings indicate low characteristic diffusivities around $10^{-6}$ m$^2$ s$^{-1}$ and correspondingly low vertical heat fluxes.

**Plain Language Summary** Ocean turbulent mixing plays an important role in the uptake and redistribution of heat, carbon, nutrients, oxygen and other properties. For example, this process delivers nutrients to the sunlit surface ocean where they are utilized to produce plants (phytoplankton) for the ecosystem food web. However, strong changes in density within the upper Arctic Ocean hinder vertical transport of nutrients, such that nutrient fluxes are generally smaller than those observed elsewhere in the world ocean. Furthermore, low vertical transport rates isolate the surface ocean from heat input from below which helps protect the ice from melting. Here, we compare the strength of upper ocean mixing, an important parameter for the calculation of vertical transport, derived from two independent methods during the MOSAiC (Multidisciplinary drifting Observatory for the Study of Arctic Climate) ice drift experiment, 2019–2020. This comparison allows us to better quantify the vertical diffusivity, and in turn also the vertical transport of for example, heat and nutrients in the ocean.

## 1. Introduction

Ocean turbulent mixing plays an important role in the uptake and redistribution of heat, carbon, nutrients, oxygen and other dissolved gasses. To quantify vertical turbulent transport, a reliable estimate of the turbulent diffusivity, $K_z$, is required. Numerous approaches have been applied to ascertain $K_z$ in the upper ocean, including the use of naturally occurring isotopes such as $^{228}$Ra (Hsieh et al., 2021), $^{7}$Be (Kadko & Johns, 2011; Kadko et al., 2020), $^{32}$P (Lee et al., 1991), tracer release experiments using fluorescent dye (Vasholz & Crawford, 1985) and SF6 (Holtermann et al., 2012a, 2012b; Ledwell et al., 1998, 2008, 2011), and turbulence measurements with microstructure profilers (e.g., in the Arctic Ocean, Fer, 2009; Lenn et al., 2009; Rainville & Winsor, 2008; Schulz, Janout, et al., 2021; Sirevaag & Fer, 2012). These methods involve observations and estimates made over largely different spatial and temporal scales, and there have been relatively few inter-comparisons of these approaches at any one time and place (e.g., Gregg et al., 2018). Especially in the Arctic Ocean, where observations are scarce and the turbulent mixing regime is distinctly different from other oceanic environments, the reliable quantification of $K_z$ poses a challenge.

In most parts of the Arctic Ocean, and especially in the deep basin, a cold halocline isolates the surface layer and ice from heat stored in the Atlantic Water layer (e.g., Carmack et al., 2015). However, with the receding sea ice cover on a pan-Arctic scale, an increased transfer of momentum from the atmosphere to the ocean is possible, with the potential to enhance vertical turbulent diffusion. The combined effect of receding ice cover and other trends in the Arctic System, for example, changes in the freshwater dynamics, on turbulent transport is not conclusively understood, and might be regionally and seasonally different. No pronounced trends are reported in the western Arctic Ocean (Dosser et al., 2021; Fine & Cole, 2022), while stronger changes are observed in the eastern Arctic Ocean, especially during summer season (Dosser et al., 2021). The region along the continental slopes of the eastern Arctic Ocean, from the Kara Sea to the Siberian Seas, is subject to Atlantification (Polyakov et al., 2017), that is, an eastward progression of conditions typical for the Atlantic Ocean. This process is associated with a weakening of the halocline, a shoaling of the Atlantic water layer, and an increase in turbulent mixing. In fact, levels of turbulence in the Eurasian Basin have increased over the last decade (Polyakov, Rippeth, Fer, Baumann, et al., 2020; Schulz, Janout, et al., 2021), resulting in a substantial increase of upward oceanic heat flux (Polyakov, Rippeth, Fer, Alkire, et al., 2020). Especially in the generally more energetic regions above the continental slope (Rippeth et al., 2015), vertical transport might increase with receding sea ice cover (Schulz, Büttner, et al., 2021).

Furthermore, the central Arctic is oligotrophic and remote from land-derived nutrient inputs, and water located at intermediate depths below the euphotic zone is the main source of nutrients. Vertical mixing can hence be a significant source of nutrients (Hsieh et al., 2021; Kadko et al., 2020; Lewis et al., 1986; Oschlies, 2002; Schulz, Lincoln, et al., 2022), and upward turbulent transport of nutrients is required to drive at least part of new primary production (Ledwell et al., 2008; Painter et al., 2014; Wagener et al., 2008). Primary production is therefore limited by nutrient supply mediated by physical transport mechanisms (Tremblay et al., 2015), of which vertical mixing is a key process that will determine the fate of marine Arctic ecosystems (Ardyna et al., 2014; Babin, 2020; Schulz, Lincoln, et al., 2022). However, the steep vertical density gradients in the upper Arctic Ocean hinder vertical diffusion of nutrients, such that nitrate fluxes are on average one to two orders of magnitude smaller than those observed elsewhere in the world ocean (Randelhoff et al., 2020). A quantitative assessment of vertical diffusivity in the upper ocean is hence crucial for understanding the transport of heat and nutrients in the Arctic, especially in light of the substantial changes which are anticipated for the oceanic mixing regime (Dosser et al., 2021; Polyakov et al., 2017; Schulz, Büttner, et al., 2021; Schulz, Lincoln, et al., 2022; Timmermans & Marshall, 2020).

In this study, we compare vertical diffusion rates derived from a $^{7}$Be tracer-based approach (Sections 2.1 and 3.1) to those derived from direct turbulence measurements from a microstructure profiler (Sections 2.2 and 3.2), during the winter-time period of the year-long Multidisciplinary drifting Observatory for the Study of Arctic Climate (MOSAiC) ice drift experiment, 2019–2020. The good agreement of the two independent methods (Section 3.3) gives confidence in their applicability, and allows to derive vertical heat fluxes over the halocline region in the winter Arctic Ocean (Section 4).

## 2. Background and Methods

Data presented here were obtained during the MOSAiC expedition on board the research vessel *Polarstern*, during which the ship was locked into an ice floe and drifted across the eastern Arctic Ocean (Figure 1). An overview of the drift and the oceanographic activities during this year-long expedition can be found in Rabe et al. (2022). Here, we focus on measurements of $^{7}$Be concentration in the upper ocean (Section 2.1) and direct oceanic turbulence measurements obtained with a microstructure profiler (Section 2.2) during the first part of the drift, 24 October 2019 to 11 February 2020.

### 2.1. $K_z$ Estimates Based on $^{7}$Be Measurements

#### 2.1.1. Theory

Beryllium-7 ($^{7}$Be) is a cosmic ray–produced radioactive nuclide with a half-life of 53.3 days. It is deposited upon the Earth's surface by precipitation and homogenized within the surface mixed layer of the ocean rapidly with respect to its decay rate (e.g., Kadko & Olson, 1996; Silker, 1972; Young & Silker, 1980). In the absence of physical removal processes other than radioactive decay, the ocean's water column inventory of the isotope represents an integration of the atmospheric input flux over approximately the previous mean-life (77 days) of

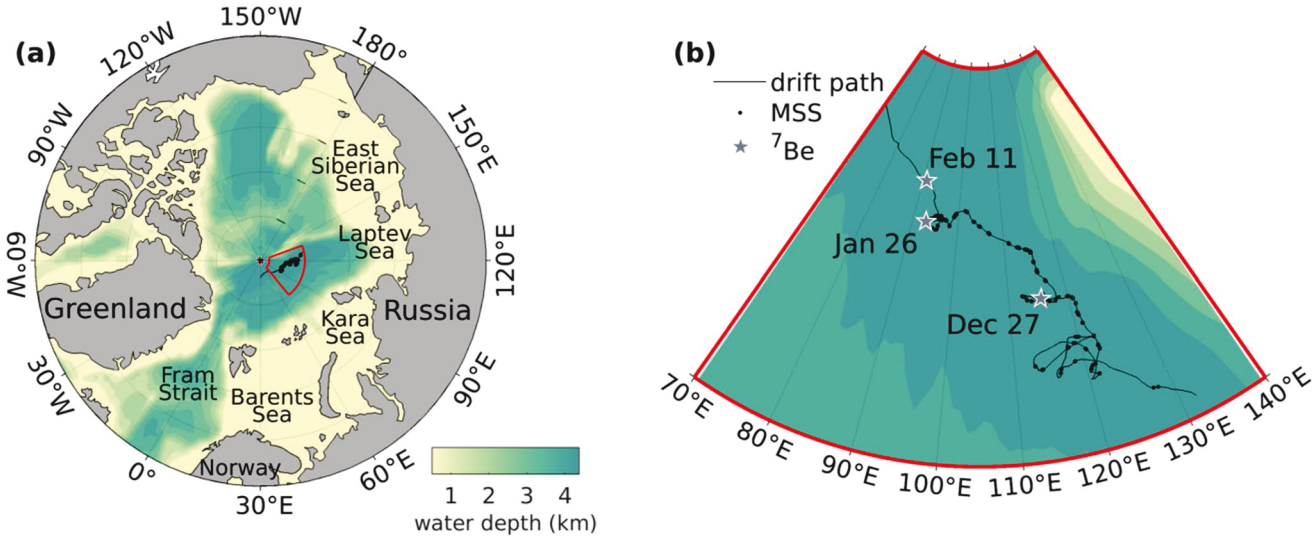


**Figure 1.** (a) Topographic map of the Arctic Ocean, with the study area (red) and sampling stations (black dots) indicated. (b) Enlargement of the study region, with cruise track (black line), turbulence profile sampling stations (black dots, "MSS," until 11 February 2020) and $^{7}$Be profile locations (gray stars) indicated.

the isotope (e.g., Aaboe et al., 1981; Kadko & Johns, 2011; Kadko et al., 2016). The $^{7}$Be input flux to the ocean ($F$) and water column $^{7}$Be inventory ($\sum^{7}$Be) varies as a function of precipitation, and is relatively constant over broad oceanic regions (Kadko & Johns, 2011; Kadko & Olson, 1996; Young & Silker, 1980). Concentration ($C$) units of $^{7}$Be are in disintegrations per minute per m$^3$ (dpm m$^{-3}$), and units of $\sum^{7}$Be, the integrated standing crop (inventory) of $^{7}$Be in the surface ocean (i.e., the integral of the concentration over the depth of the water column) are in dpm m$^{-2}$.

The standing crop of $^{7}$Be is insensitive to short-term (daily to weekly) variability of $^{7}$Be input, since $^{7}$Be has a seasonal mean life, lending to the system an inertia with respect to short term input events. However, in the Arctic, $F$ becomes zero upon establishment of the ice cover which coincides with the late-summer freeze-up. The ocean $^{7}$Be thereafter decays radioactively, with a decay constant of $\lambda = 0.013$ days$^{-1}$.

The relative concentration of $^{7}$Be in the mixed layer and below, and the shape of the "tail" below the mixed layer, provide information on the strength of the local vertical mixing and the vertical diffusivity $K_z$ (Haskell II et al., 2015; Kadko & Johns, 2011). Assuming $F = 0$ (appropriate for ice-covered conditions), a surface mixed layer of constant depth $H$, in which $^{7}$Be concentration is homogeneous, that is, no vertical gradients, and an initial surface layer concentration $C_0$ at the time of freeze-up, the temporal evolution of the surface layer $^{7}$Be inventory satisfies

$$H\frac{\partial C}{\partial t} = -K_z\frac{\partial C}{\partial z}\bigg|_H - \lambda C_0 H, \tag{1}$$

where the first term on the right hand side is the flux through the base of the mixed layer. In the layer below, the temporal evolution and vertical distribution of $^{7}$Be is determined by vertical diffusion and radioactive decay over time as

$$\frac{\partial C}{\partial t} = K_z\frac{\partial^2 C}{\partial^2 z} - \lambda C, \tag{2}$$

where the vertical diffusivity is assumed constant with depth. The model is initialized with the $^{7}$Be concentration at freeze-up ($C_0$) uniformly distributed in the surface layer, and zero concentration below. The lower boundary at 150 m was chosen deep enough to avoid non-zero $^{7}$Be concentrations in its vicinity. Horizontal advection and non-conservative reaction terms are not considered in this formulation. Equations (1) and (2) are numerically solved with a time step of 7.2 min, starting at the time of freeze-up, and a vertical resolution of 1 m. The mixed layer concentration is homogenized at each time step. The model was run with different realizations of constant $K_z$ with an increment of $0.05 \times 10^{-6}$ m$^2$ s$^{-1}$, and the best fit (in the least-squares sense) was determined by comparing simulated profiles with the respective measured $^{7}$Be concentration profile (see Figure 3 in Section 3.1).

The approach used here is similar to that described for $^{7}$Be data collected during the 1997 SHEBA (Surface Heat Budget of the Arctic Ocean) experiment (Kadko et al., 2020). However, for the SHEBA data a 40 m shoaling of the mixed layer during the spring to summer transition had to be accounted for in the modeling approach. This is not the case for the mid-winter interval studied here, where the mixed layer depth was relatively constant at ∼30 m during the considered study period (October 2019 to February 2020).

#### 2.1.2. Measurements

During MOSAiC, water column profiles for $^{7}$Be analyses were collected at the locations shown in Figure 1b. Methods for $^{7}$Be analysis have been previously described in detail (e.g., Kadko, 2000; Kadko & Swart, 2004; Kadko et al., 2016). Briefly, pumps were used to collect seawater within the upper 60 m of the ocean on 27 December 2019, January 26 and 11 February 2020. A temperature, conductivity and depth sensor was attached to the inlet of the hose to track its exact vertical position. Typically 1,400–2,100 L were taken from a hydrohole through the ice at 1–2 depths below the mixed layer. Unfiltered seawater was drawn through the sampling hose to the surface where it was passed through iron-oxide impregnated acrylic fiber filters which adsorbs the $^{7}$Be (Krishnaswami et al., 1972; Lal et al., 1988; Lee et al., 1991). A flow meter attached in-line to the filter compartment recorded the amount of seawater that passed through each filter. To maximize $^{7}$Be collection, two fibers filtering 600–700 L of seawater apiece were collected from each ice station depth and later combined. The efficiency of the fiber for extraction of Be from seawater was determined by adding stable Be atomic absorption standards to a drum containing seawater (bringing the stable Be concentration to ∼1 ppm), pumping the water through an iron fiber cartridge, and at every 100 L measuring the Be content of the cartridge effluent. Based on six trials, it was found that for sample volumes of 600 and 700 L, extraction efficiencies are 78 ± 2% to 76 ± 2%, respectively (Kadko, 2009). The uncertainty of the extraction efficiency (3%) and the detector efficiency (2%) was, in all cases, smaller than the statistical counting error and the uncertainty in the blank. For the mixed layer samples, water was collected from the ship's seawater intake at ∼8 m water depth and collected in barrels from which the water was passed through the iron-oxide filters as described above. The fibers were dried and shipped to Florida International University. There, the fibers were ashed, placed in a Marinelli beaker, and analyzed with a high purity germanium (HPGe) gamma detector (Kadko et al., 2016). The $^{7}$Be has a readily identifiable gamma peak at 478 keV. The detector is calibrated by adding a commercially prepared mixed solution of known gamma activities to an ashed fiber and counting it in the Marinelli geometry.

### 2.2. $K_z$ Estimates Based on Dissipation Rate Measurements

#### 2.2.1. Theory

Small-scale turbulent kinetic energy (TKE) in the ocean is produced by current velocity shear, mainly associated with internal waves, and is largely dissipated by viscous friction. The TKE dissipation rate per unit mass is denoted by $\varepsilon$ (W kg$^{-1}$). Small scale velocity fluctuations can be directly measured with airfoil shear probes which, when mounted on a platform that descends slowly and undisturbed through the water column, measure profiles of the vertical shear $\frac{\partial u}{\partial z}$, with $u$ being the horizontal current velocity and $z$ being the vertical coordinate. Under the assumptions of isotropic turbulence, that is, that turbulent motions are statistically uniform in all directions, the dissipation rate of TKE can be calculated as

$$\varepsilon = 7.5\nu\left\langle\left(\frac{\partial u}{\partial z}\right)^2\right\rangle, \tag{3}$$

where $\nu$ is the kinematic molecular viscosity, $\frac{\partial u}{\partial z}$ is the vertical shear resolved from $\mathcal{O}$(1 m) to $\mathcal{O}$(1 cm) scales, and $\langle . \rangle$ denotes averaging. However, a fraction of the TKE is not dissipated by friction but used to mix the fluid by inducing a net buoyancy flux. This vertical mixing can be quantified as the vertical turbulent diffusivity $K_z$.

A widely accepted parameterization of $K_z$ is provided in Bouffard and Boegman (2013). The authors identify four mixing regimes, characterized by the buoyancy Reynolds number

$$Re_b = \frac{\varepsilon}{\nu N^2}, \tag{4}$$

where $N$ is the buoyancy frequency, and derive a corresponding parameterizations of $K_z$ (Equation 5). In the molecular regime, $\mathrm{Re}_b < 1.7$, that is, in quiescent conditions, molecular diffusion dominates and $K_z$ equals to the molecular diffusivity $K_m$. At slightly higher $\mathrm{Re}_b \leq 8.5$, strong stratification suppresses turbulent mixing and

$K_z$ scales with $Re_b^{1.5}$ (buoyancy controlled regime). In the transitional regime $8.5 < \mathrm{Re}_b \leq 400$, $K_z$ was found to linearly depend on $\mathrm{Re}_b$, corresponding to a previous parameterization following Osborn (1980), using a constant mixing coefficient of $\Gamma = 0.2$. In the energetic regime $\mathrm{Re}_b \geq 400$, $\Gamma = 0.2$ is an overestimate, and a better agreement was found for $K_z \sim Re_b^{0.5}$:

$$K_z = \begin{cases} K_m, & Re_b \leq 1.7 \\ 0.0615 \nu Re_b^{1.5}, & 1.7 < Re_b \leq 8.5 \\ \Gamma \nu Re_b, & 8.5 < Re_b \leq 400 \\ 4 \nu Re_b^{0.5}, & Re_b \geq 400. \end{cases} \tag{5}$$

### 2.2.2. Measurements

During MOSAiC, high resolution vertical profiles of temperature, salinity and shear velocity were performed with a loosely tethered microstructure profiler (MSS90L, Sea and Sun Technology, Germany, sampling frequency 1,024 Hz), equipped with sensors for temperature, conductivity, and two airfoil shear probes (PNS06 from ISW, Germany), descending at a fall speed of around 0.6 m $s^{-1}$. Near-daily measurements comprising at least five consecutive profiles were performed through a hydrohole at the Ocean City site of the ice floe, ~350 m from *Polarstern*. Turbulent dissipation rates were estimated independently from both shear sensors, and all data were averaged in 1 m vertical bins. A detailed description of the sampling strategy and the data processing can be found in the data descriptor (Schulz, Mohrholz, et al., 2022).

We estimate $K_z$ using Equation 5, with $N$ being calculated from the 1-m vertical resolution profiles of conservative temperature and absolute salinity, using the TEOS-10 set of sea water equations (McDougall & Barker, 2011). The $K_z$ profiles are then extracted in the depth range comparable for the $^7$Be-based estimates, which are characteristic for the region across the mixed layer base (or mixed layer depth, MLD) and the upper cold halocline. At a depth of approximately 60 m, modeled $^7$Be concentrations are effectively zero (see Section 3.1). We hence select from each microstructure profile the data between 2 m above the MLD and 60 m depth, where the MLD is identified as the depth where the density increased by its surface value by 0.1 kg $m^{-3}$, to obtain a mean estimate of the turbulent diffusivity over this depth range.

Estimates of oceanic dissipation rates are often assumed to be approximately lognormally distributed, due to their strong intermittency in amplitude, space and time, or log-skew-normal distributed, as they are the result of several interactive turbulence processes (Cael & Mashayek, 2021). Calculating spatio-temporal averages of turbulent properties, for example, $\varepsilon$ and $K_z$, is hence not trivial, as their exact probability distribution—and therefore the appropriate averaging method—is unclear (see Figure 5 in Section 3.3 for the distribution of the data presented here). In addition to the simple arithmetic or geometric mean, an alternative averaging method is a maximum likelihood estimator (MLE) of the mean of a lognormal random variable, as described in Baker and Gibson (1987), which also provides confidence limits. In the following, we use all 1 m estimates of $\varepsilon$ and $N^2$ in the identified depth range within a given time interval (e.g., one day) to calculate averages according to the different methods (the arithmetic mean, the geometric mean, and the MLE), to discuss their respective performance, also in comparison with the $K_z$ estimates from the $^7$Be method (Sections 3.2 and 3.3).

In addition, daily estimates of vertical heat fluxes are calculated from $K_z$ values and the vertical gradient in potential temperature $\theta$, according to

$$F_h = -\rho_0 c_p K_z \frac{\partial \theta}{\partial z}, \tag{6}$$

where $\rho_0 = 1{,}027$ kg $m^{-3}$ is the reference density, and $c_p \approx 3{,}991.9$ J $kg^{-1}$ $K^{-1}$ is the specific heat capacity of sea water. The vertical temperature gradient is calculated as the difference between the surface mixed layer temperature (5–10 m depth average) and the temperature at 60 m. As the surface mixed layer temperature was homogeneous in the vertical during the investigated time period, the former value is insensitive to the exact averaging interval within the mixed layer. To calculate daily mean heat fluxes, we used the arithmetic mean of individual temperature gradients on the respective day, and the daily mean $K_z$ using the MLE averaging method as described above (see Section 3.3 below for the justification of the choice of the averaging method). The vertical axis is oriented in a way that positive values indicate an upward heat flux.

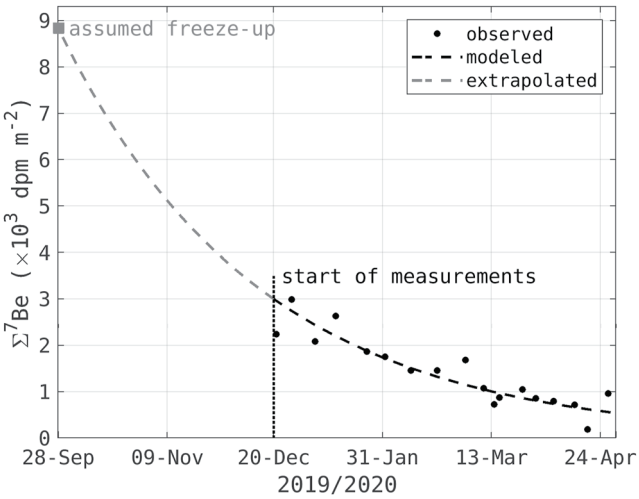


**Figure 2.** Measured $^{7}$Be ocean inventory (black dots), the inventory's modeled decline (dashed black line), and the extrapolated inventory to the past from the start of sampling to the assumed time of freeze-up (dashed gray line).

## 3. Results and Discussion

### 3.1. $K_z$ Estimates Based on $^{7}$Be Measurements

The inventory of $^{7}$Be, starting from the first measurement on 21 December 2019, declined exponentially throughout the measurement period with the fitted time constant equaling the radioactive decay constant of $^{7}$Be of 0.013 days$^{-1}$ (Figure 2). This suggests that after freeze-up, the water column was isolated from air-sea exchange, that is, zero $^{7}$Be flux into the water column, and that $^{7}$Be was removed solely by radioactive decay. This justifies the assumptions summarized in Section 2.1, that is, no horizontal effects or non-conservative behavior. The exponential relationship can be extrapolated to the time of freeze-up (Figure 2). Here, we choose 28 September 2019 as the freeze-up date based on the observation that there was full ice coverage at the start of the MOSAiC drift on 4 October 2019 (Krumpen et al., 2021) and the yearly ice minimum was reached 18 September 2019. The ocean $^{7}$Be inventory extrapolated to September 28 was 8,880 dpm m$^{-2}$ (Figure 2), which is comparable to values reported in other studies: The total $^{7}$Be inventory across the US GEOTRACES transect (Makarov and Canada Basins) ranged between 4,600 and 8,800 dpm m$^{-2}$ (Kadko et al., 2019), for the Eastern Central Arctic a range of 5,500–13,000 dpm m$^{-2}$ was reported (Kadko et al., 2016), and Cámara-Mor et al. (2011) reported a value of 7,800 dpm m$^{-2}$ for a transect in the Eurasian Basin.

Estimates of vertical diffusivity from the $^{7}$Be method include a typical uncertainty of 50%–60% associated with the decay of $^{7}$Be concentrations during the time between sample collection and analysis, error

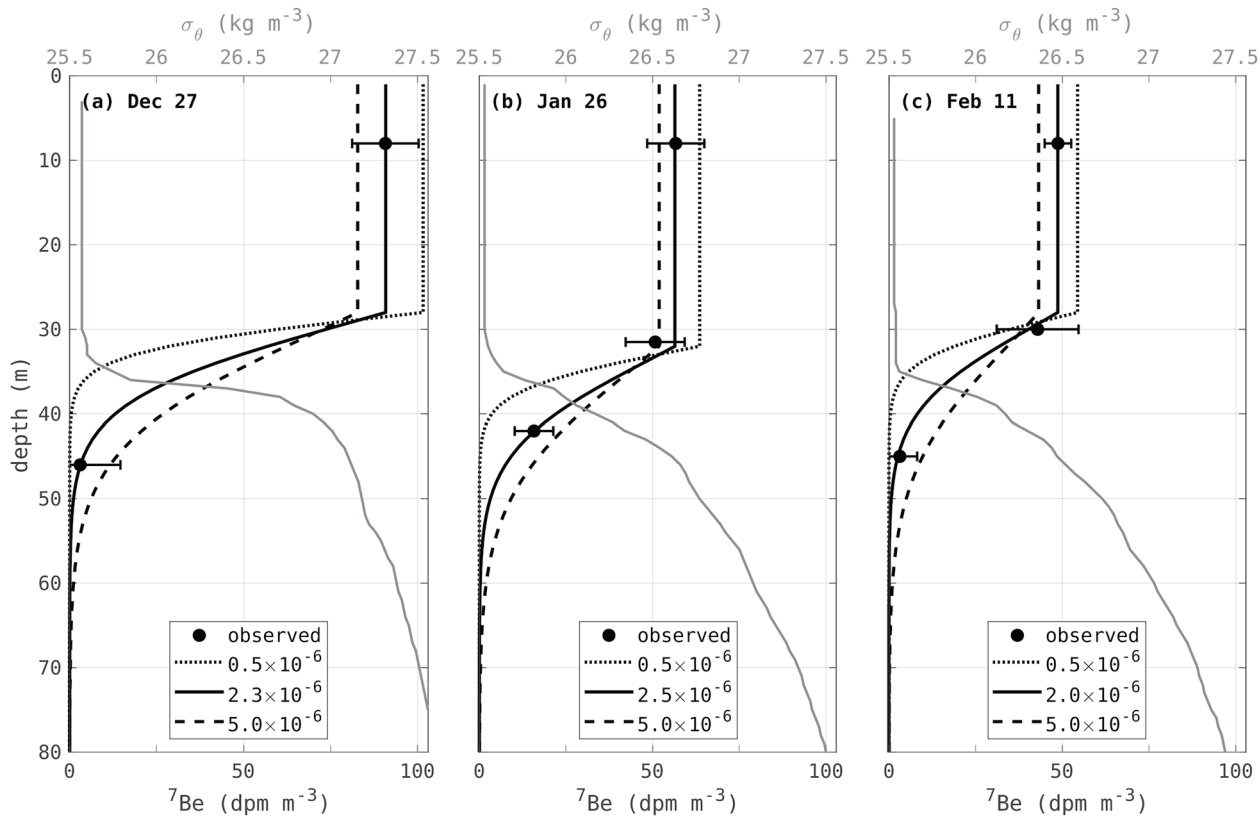


**Figure 3.** $^{7}$Be activities plotted versus depth for (a) 27 December 2019; (b) 26 January 2020; and (c) 11 February 2020. Model fits with variable $K_z$ (in m$^2$ s$^{-1}$) as indicated are shown, and best fits are indicated in solid lines.

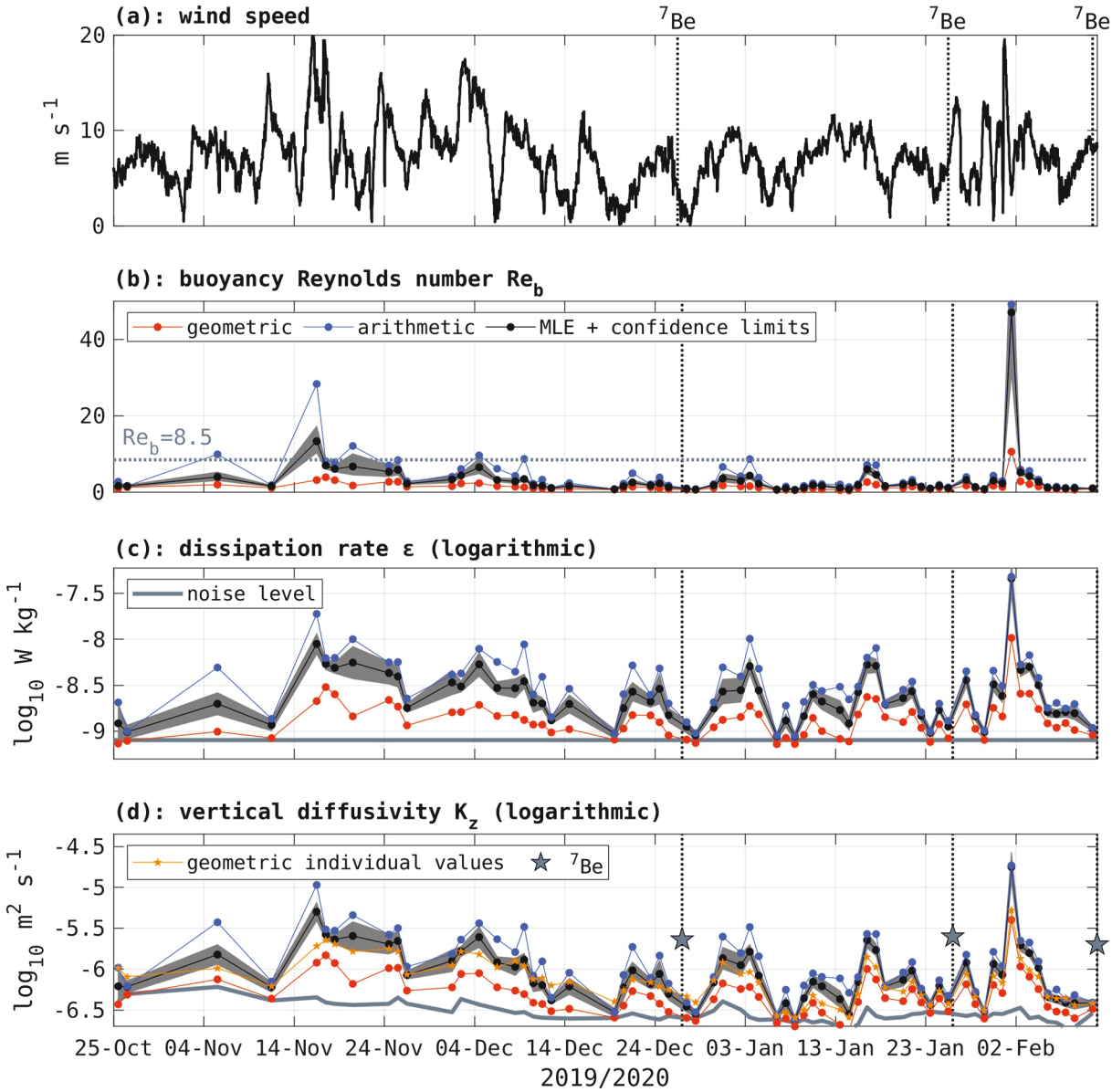


**Figure 4.** (a) Wind speed measured at RV Polarstern, with temporal resolution of 30 min; daily averages of the upper ocean cold halocline layer (b) buoyancy Reynolds number, (c) turbulent dissipation rate, and (d) turbulent diffusivities. Line colors indicate values calculated from the geometric mean of $\varepsilon$ (orange), the respective arithmetic mean (blue), and as maximum likelihood estimator (black) with 95% confidence limits (gray shading). Gray lines in (c) and (d) denote the noise level. In (d), stars indicate the $K_z$ estimates from the $^7$Be method, and the orange lines with stars as markers are the geometric averages calculated from profile-averaged $K_z$ estimates.

propagating in the calculations, and the curve fitting method (Haskell II et al., 2015). The individual estimates derived from the three $^7$Be profiles are found to be $K_z = 2.3(\pm1.4) \times 10^{-6}$ m$^2$ s$^{-1}$ (27 December 2019), $2.5(\pm1.4) \times 10^{-6}$ m$^2$ s$^{-1}$ (26 January 2020), and $2.0(\pm1.1) \times 10^{-6}$ m$^2$ s$^{-1}$ (11 February 2020). These estimated values of $K_z \sim 2 \times 10^{-6}$ m$^2$ s$^{-1}$ from the $^7$Be profile measurements (Figure 3) are similar to those determined by $^7$Be samples during the 1997 SHEBA experiment (Kadko, 2000).

### 3.2. $K_z$ Estimates Based on Direct Turbulence Measurements

Microstructure measurements provide near-daily averages of turbulent dissipation rate $\varepsilon$ and vertical diffusivity $K_z$ (Figures 4c and 4d). As outlined in Section 2.2, and discussed in depth in Baker and Gibson (1987), estimates of $\varepsilon$, and hence the buoyancy Reynolds number Re$_b$ (Figure 4b) and $K_z$, are sensitive to the applied spatio-temporal averaging method. Qualitatively, estimates from all three averaging methods (arithmetic mean,

**Table 1**
*$K_z$ ($\times 10^{-6}$ m$^2$ s$^{-1}$) Estimates Derived From the $^7$Be Tracer Method, and From Turbulence Measurements, Averaged Over Indicated Time Periods, Using the MLE Averaging Method Outlined in Section 2.2*

| | | Microstructure measurements averaged over | | | |
|---|---|---|---|---|---|
| Date | $^7$Be | 7 days | 14 days | 30 days | 77 days[a] |
| 7 Dec 2019 | 2.3 ± 1.4 | 1.24 [1.13, 1.36] | 1.01 [0.93, 1.10] | 1.16 [1.11, 1.21] | **1.58** [1.51, 1.64] |
| 26 Jan 2020 | 2.5 ± 1.4 | 0.71 [0.67, 0.74] | 0.87 [0.83, 0.90] | 0.81 [0.79, 0.84] | **1.12** [1.09, 1.15] |
| 11 Feb 2020 | 2.0 ± 1.1 | 0.63 [0.60 0.66] | 1.13 [1.08 1.18] | 1.01 [0.98, 1.04] | **0.99** [0.96, 1.01] |

*Note.* Numbers in brackets indicate the corresponding confidence limits. Bold numbers are the averages over the half-life time of $^7$Be.

[a]Or time period from earliest available measurement on 25 October 2019.

geometric mean and the maximum likelihood estimator, MLE) exhibit the same behavior: dissipation rate values are generally low, $<10^{-8}$ W kg$^{-1}$, often close to the noise level (gray horizontal line, Figure 4c), except for a storm event in mid-November 2019 and, more pronounced, a storm event beginning of February 2020 with wind speeds up to 20 m s$^{-1}$ (Figure 4a). Regardless of the averaging method, buoyancy Reynolds numbers (Figure 4b) are mostly below 8.5, indicative of the buoyancy-controlled mixing regime (Section 2.2.1), except during the storm events. Vertical diffusivities (Figure 4d) display a similar behavior as the turbulent dissipation rates. We found a weak correlation ($R^2 = 0.49$) between daily averaged vertical diffusivities (using the MLE) and wind speeds averaged over the previous day.

As expected, $K_z$ values calculated using the arithmetic mean of $\varepsilon$ (blue lines in Figure 4) are higher than those using the geometric mean (orange lines), on average by a factor of 2, but up to a factor of 7 when comparing individual daily estimates. Estimates using the MLE method (black lines with confidence limits in gray shading) range in between the geometric and arithmetic estimates. The geometric average taken over the daily mean (geometric) averages (as opposed to taking the geometric mean of all point values in the defined depth- and time-range) are relatively close to the MLE values. In comparison to the MLE long-term average of 77 days (the half-life time of $^7$Be, see Section 3.3 and Table 1), using the geometric mean systematically underestimates vertical diffusivities by ∼50%, while using the arithmetic mean results in an overestimation of around 70%–80%. Applying the geometric mean to the daily (geometric) average with the respective time span results in turbulent diffusivities which are less than 20% smaller than those obtained with the MLE method.

Another uncertainty arises from the choice of the vertical range (2 m above the depth of the mixed layer, located at approximately 30 m depth, to 60 m depth) used for the average. Again relative to the MLE long-term average of 77 days, vertical diffusivities are most sensitive to the choice of the upper bound. Averages starting at 5 m above the mixed layer depth (as opposed to 2 m) result in higher average diffusivities of +3, +29, and +50%, corresponding to the three time periods corresponding to the available $^7$Be measurements. An increase of the vertical interval from 60 m to the lower bound of the halocline (mean and standard deviation 77 ± 8 m, based in a density ratio criterion as defined in Bourgain and Gascard (2011)), results in a change in $K_z$ of less than 10%. The effect of changing the density threshold used to determine the mixed layer depth from $\Delta\sigma = 0.1$ kg m$^{-3}$ to 0.2 kg m$^{-3}$ on the $K_z$ estimates is −12%–14%.

### 3.3. Method Comparison

The $K_z$ estimates based on measured turbulence profiles reflect instantaneous conditions, while the $^7$Be method integrates over a longer period of time in the order of the isotope mean life of 77 days, and thus has a "memory" of earlier events. To account for the longer integration period reflected in the $^7$Be-based $K_z$ estimates, data were averaged over the 7, 14, 30, and 77 days preceding the $^7$Be sampling day for the method comparison (Table 1), thereby using the different averaging methods outlined in Section 2.2.2 on all data points that fall in the specified depth- and time-range. The long term, 77 days, $K_z$ averages from the dissipation rate profiles, using the MLE averaging method, are generally smaller, but within the uncertainty margins of the $K_z$ estimates from the $^7$Be method (Figure 5, Table 1).

Shorter averaging time periods of $K_z$ estimates from turbulence profiles include for example, short term storm events (beginning of February, see Figure 4), and result in more variable values and an overall worse agreement

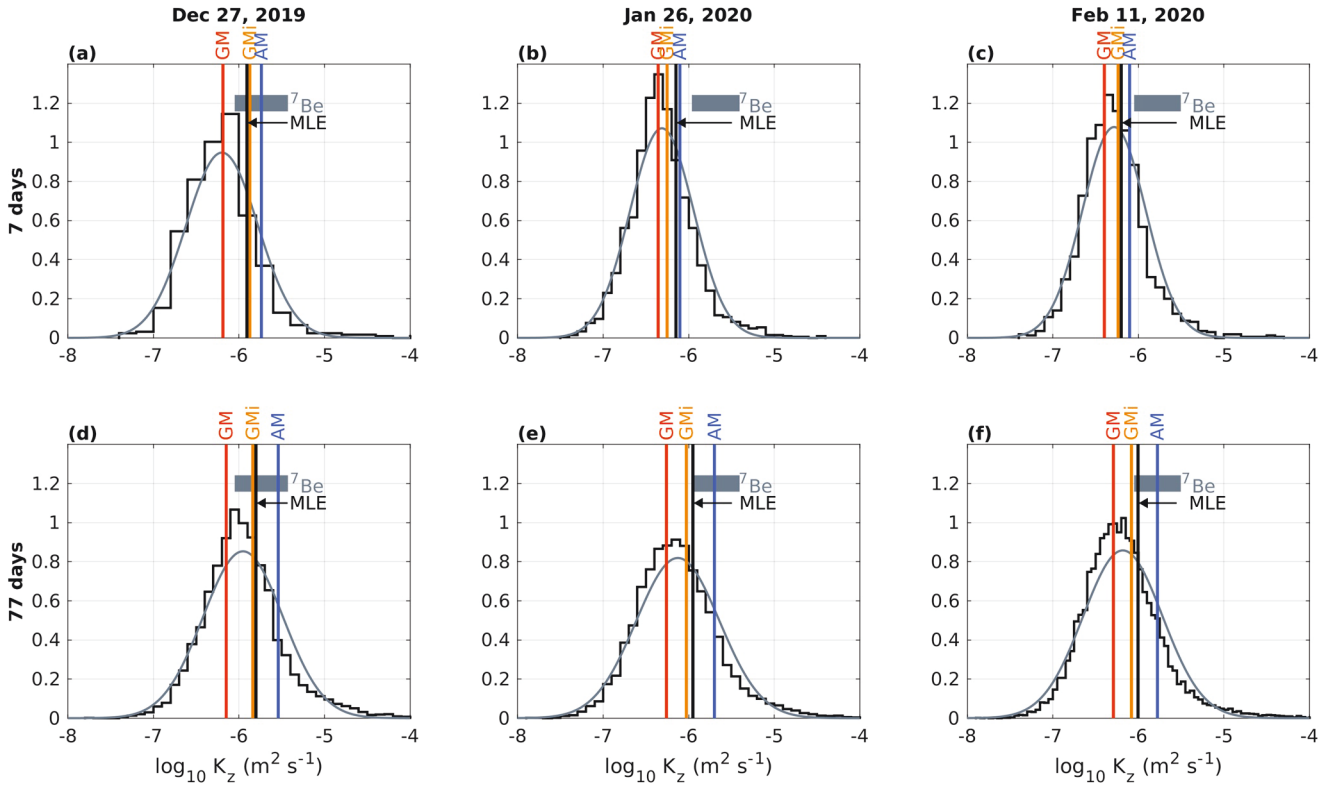


**Figure 5.** Probability density function estimates for individual 1 m $K_z$ values from the microstructure profiles in the here considered depth range (black lines) within (a)–(c) 7 days and (d)–(f) 77 days before the $^7$Be measurements in (a), (d) December, (b), (e) January and (c), (f) February. Gray patches indicate the (uncertainty) range of the respective $K_z$ estimates based on the $^7$Be method, vertical lines indicate $K_z$ estimates from the microstructure measurement over the respective time period, using different averaging methods: The geometric mean (GM, dark orange lines), the arithmetic mean (AM, blue lines), geometric means of profile-average values (GMi, light orange), and the maximum likelihood estimator (MLE, black lines). Gray lines show lognormal probability density functions fitted to the data displayed. The Lillefors test indicates that none of the data subsets is lognormal-distributed at any significance level.

with the $^7$Be method (Figure 5, Table 1). Given the long integrated time period associated with the estimates from the $^7$Be method, this result is not surprising, but underlines the importance of long time series to accurately estimate a representative vertical diffusivity from turbulence measurements. In turn, the $^7$Be method does not reflect the intermittency of turbulent mixing and its response to short term forcing like the storm event in February.

Overall, the two independent methods point to a vertical diffusivity in the winter Arctic Ocean upper ocean halocline of approximately $10^{-6}$ m$^2$ s$^{-1}$, with an uncertainty of around factor 2. This value is well in line with previous estimates of turbulent diffusivities in the Arctic Ocean, and especially the halocline, being low compared to other oceanic regions (e.g., Fer, 2009; Shaw & Stanton, 2014).

## 4. Application: Vertical Heat Fluxes

The robust estimates of the turbulent diffusivity presented in the previous section allow for the calculation of vertical fluxes of for example, heat or, with additional data sets, other tracers such as oxygen or nutrients. In the following, we will present and discuss heat flux estimates corresponding to the time period (winter) and vertical range (upper halocline) of the $K_z$ estimates presented in this study. Heat fluxes over this depth range characterize the exchange between the interior ocean, via the strongly stratified halocline, and the surface mixed layer, and are hence an important parameter for understanding surface layer exchange and energy dynamics, for example, the ice mass balance.

Upper ocean winter heat fluxes in the central Amundsen Basin are generally very low (Figure 6a). On 80% of in total 66 observational days, the absolute value of the average heat flux is smaller than 0.01 W m$^{-2}$, and slightly higher, between 0.02 and 0.05 W m$^{-2}$, on 18% of the days (Figure 7). These slightly higher heat fluxes mostly

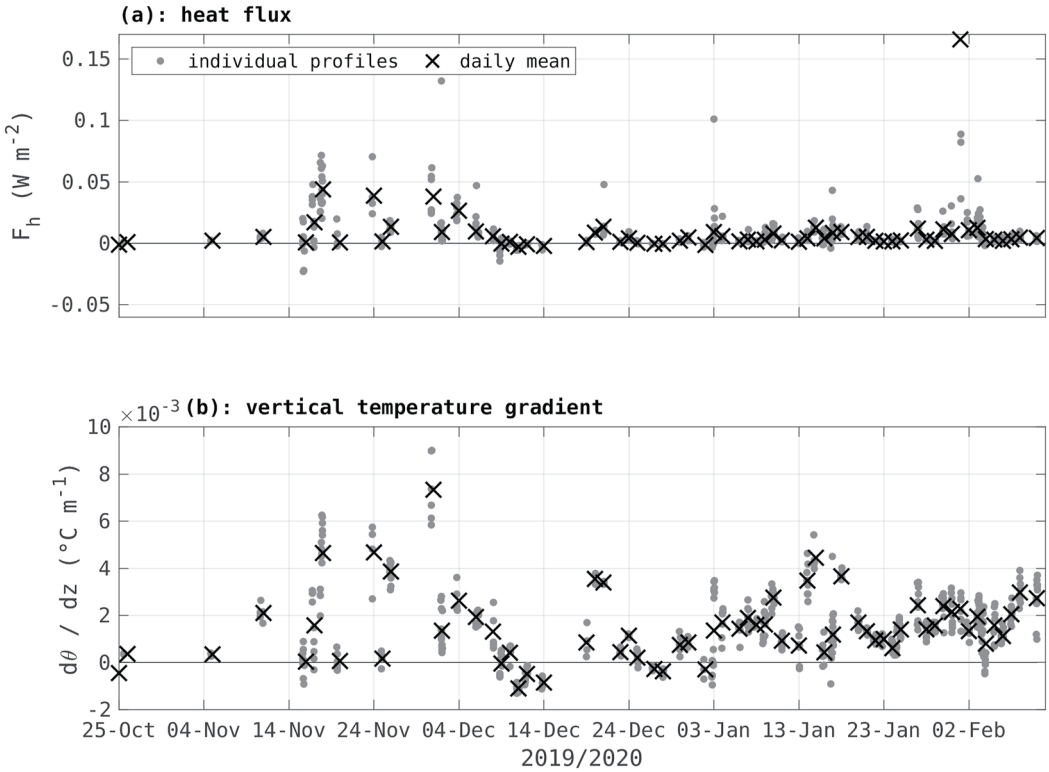


**Figure 6.** (a) Upper ocean vertical heat fluxes (positive is upwards), and (b) vertical temperature gradient, calculated from individual profiles (gray dots) and daily mean values (black crosses). The vertical axis was limited to better display variability at low values, some heat fluxes from individual profiles on February 2 are higher than the vertical axis limit.

occurred during the second half of November 2019, when the surface mixed layer depth was relatively variable and upper ocean temperature profiles were characterized by layers of temperature anomalies and inversions. These oceanic conditions might be a result of more dynamic ice conditions during that time, associated with the presence of a low pressure system between 16 November 2019 and 19 November 2019 (see cruise reports for details), causing for example, the opening of an approximately 20 m wide lead close to the microstructure profile sampling location on November 16 (Schulz, Mohrholz, et al., 2022). Only on 1 February 2020, a higher daily averaged heat flux of 0.17 W m$^{-2}$, directed upwards, was recorded, caused by elevated levels of turbulent mixing associated with a storm event.

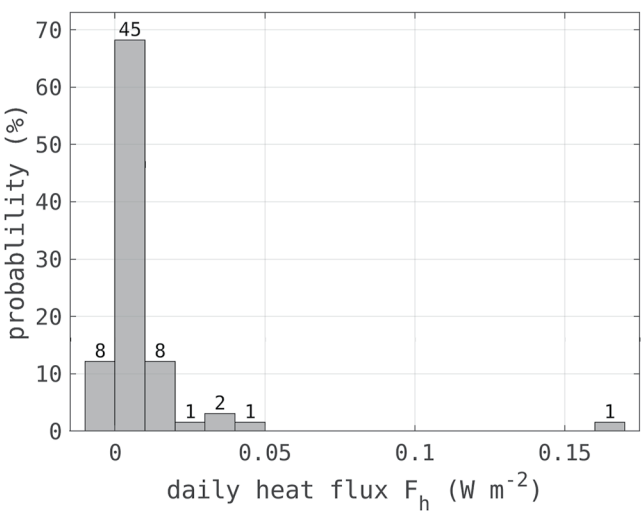


**Figure 7.** Probability distribution of daily average heat fluxes. Number above the bars indicates the number of days (out of 66 days total) with heat fluxes in the respective interval.

It is noteworthy that especially in the presence of temperature inversion layers and intrusions below the well mixed surface layer, the orientation of vertical heat fluxes is sensitive to the chosen depth range over which the temperature gradient is calculated. Heat fluxes based on temperature gradients calculated as a linear regression, that is, estimating the temperature gradient as the slope of a least-squares fit of the temperature as a function of depth, for example, over the depth range considered for the $K_z$ estimates, have no distinct vertical orientation. For more detailed investigations of shorter time periods, the depth range over which heat fluxes are calculated needs to be carefully chosen, taking into account the finer scale vertical temperature stratification, to provide a parameter suitable to address the specific research topic in consideration. However, the overall estimate of low heat fluxes in the order of ±0.01 W m$^{-2}$ is insensitive to the exact choice of the depth interval.

The presented approach of calculating heat fluxes based on a spatial mean diffusivity and an average temperature gradient does not account for potential correlations between the two parameters. To include these correlations, an

alternative approach is to simply average all heat fluxes (within the desired depth interval) calculated using $K_z$ and $\frac{\partial\theta}{\partial z}$ data on the provided 1 m vertical resolution. The disadvantage of this approach is that individual heat fluxes on 1 m resolution rely on a single estimate of $K_z$, which is—as all turbulence parameters—subject to measurement uncertainties, and outliers can distort the average heat flux. Comparing heat fluxes for all considered profiles reveals that simply averaging heat fluxes leads to a slightly larger spread of values, and a deviation from the bulk heat fluxes as presented here by on average a factor 2. Still, 89% of profile averaged heat fluxes using this alternative approach are smaller than 0.05 W $m^{-2}$, confirming that heat fluxes over the winter Arctic halocline are very small. Which averaging method is more appropriate ultimately depends on the scientific question, that is, the vertical scale which should be represented, and the structure of the water column, for example, the presence or absence of considerable small-scale temperature gradients.

To the authors knowledge, the only direct observations of winter heat fluxes derived from microstructure shear measurements are available from the extensive N-ICE campaign in 2015 north of Svalbard (Meyer et al., 2017). There, average heat fluxes over the pycnocline were much larger than the values reported here, around 3 W $m^{-2}$ and strongly enhanced during storm events (Meyer et al., 2017). Oceanic heat flux was also measured by eddy-covariance method in the under-ice boundary layer during the N-ICE 2015 experiment. In winter, during the drift over the Nansen Basin from January to March, average ocean-to-ice heat flux was weakly positive during quiescent conditions ($1.0 \pm 1.1$ W $m^{-2}$), increasing to $2.1 \pm 2.3$ W $m^{-2}$ when averaged over storm periods. The large standard deviation reflects the large temporal variability of near-zero values (Peterson et al., 2017). However, the winter water column structure during N-ICE was characterized by a much deeper, on average 93 m, surface mixed layer, compared to around 30 m for the data presented here. Furthermore, the Atlantic water layer was much shallower, with the 0°-isotherm located at ∼100 m, compared to approximately 140 m here. The properties of the much thinner halocline encountered during N-ICE are, therefore, not comparable to those of the pronounced halocline in the central Amundsen Basin. The comparison of winter heat fluxes from N-ICE and MOSAiC highlights the structural differences between the relatively energetic region with a shallow Atlantic Water layer characterized by complex topography north of Svalbard, where Atlantic water heat can be transported to the surface layer relatively easily, and the quiescent basin further away from the source of Atlantic Water, where a thick and stably stratified halocline effectively blocks upward heat transfer.

Further winter heat flux estimates in the Arctic halocline are available from the SHEBA campaign in the Western Arctic (1997–1998), based on temperature microstructure measurements. Diffusivities in the halocline of the Canada Basin are found to be close to the molecular level, and vertical heat fluxes into the surface mixed layer are correspondingly small, around 0.1 W $m^{-2}$ (Shaw & Stanton, 2014). In contrast to the situation encountered during the MOSAiC reported here, the water column structure in the Canada Basin during SHEBA was characterized by distinct temperature maxima right below the surface mixed layer, associated with trapped solar insolation by summer meltwater.

Within the surface mixed layer (winter) ocean heat fluxes at fixed depth levels are available from Autonomous Ocean Flux Buoys (AOFBs), see for example, Stanton et al. (2012). The fluxes derived from AOFB deployments describe heat transport close to the ice-ocean interface, using temporal temperature fluctuations, and are hence not directly comparable with heat fluxes in the halocline layer below, as discussed in this study. However, AOFBs were also deployed during the MOSAiC drift (Rabe et al., 2022), and a comparison of the heat flux estimates from both methods in future work will provide further insights on the oceanic heat transport in the Arctic Ocean.

## 5. Outlook and Conclusions

We compared vertical diffusion rates in the upper Arctic Ocean halocline derived from a tracer method with estimates derived from microstructure measurements during the MOSAiC campaign in winter 2019/2020 in the central Amundsen basin. Such inter-comparison studies are rare, and to our knowledge have heretofore never been done in the Arctic Ocean. Estimates from both methods are found to be in good qualitative and quantitative agreement, and indicate a low characteristic vertical diffusivity on the order of $K_z = 10^{-6}$ $m^2$ $s^{-1}$. Corresponding vertical heat fluxes are not significantly different than nil. The short-term effect of dynamic sea ice conditions and storm events on $K_z$ and vertical heat fluxes is detectable, but not very pronounced, and focused cross-disciplinary investigations are needed to determine the importance of short-term variability of $K_z$ on the coupled ice-ocean system.

Our findings underline the notion that the Arctic Ocean halocline is a "bottleneck" for vertical turbulent transport and effectively shelters the sea ice and surface layer from the ocean below (Fer, 2009). However, the reported low turbulent diffusivity is only representative for winter conditions in the central Eurasian Basin. Other parts of the Arctic Ocean, for example, the more energetic continental slope regions or areas closer to the Atlantic Water inflow, display distinctly different characteristics with respect to the water column structure and vertical transport (Fer et al., 2020; Meyer et al., 2017; Schulz, Büttner, et al., 2021). Later records from the MOSAiC data set also indicate strong seasonal variability. In March, surface salinity along the MOSAiC drift has increased to a level typically present below the halocline, hence reducing upper ocean stratification and potentially altering transport dynamics. The effect of this evolution with respect to transport budget needs to be assessed in future detailed studies.

Our analysis furthermore illustrates the challenges associated with the interpretation of oceanic turbulence measurements. Averaged quantities are sensitive to the choice of the averaging method, and both the arithmetic and geometric mean result in questionable estimates. Based on the favorable comparison between the profile and tracer based estimates, we propose that the MLE of the mean from a lognormal distribution is representative of the averaging accounting for history of turbulence mixing events. Further uncertainties, especially in the calculation of vertical fluxes, arise when parameters sensitively depend on the vertical limits of the layer chosen for calculating bulk values. The determination of said layer depends on the specific problem investigated and needs to be chosen carefully to obtain a representative parameter.

The method comparison performed in this study underlines the importance of an adequate sampling strategy when investigating turbulent transport. The highly intermittent nature of turbulence requires both long sampling periods to obtain representative average values, and a high sampling frequency to capture short-term variability in response to environmental forcing. Especially in the rapidly changing Arctic, repeated sampling campaigns are necessary to assess the response of turbulent transport to climate change, as vertical mixing in the Arctic Ocean is expected to increase in response to trends in the environmental conditions, with implications for the future maintenance of sea ice and Arctic Ocean primary production (e.g., Rippeth & Fine, 2022).

## Data Availability Statement

Observational data used in this study is available at Schulz, Mohrholz, et al. (2022b) via https://doi.org/10.1594/PANGAEA.939816 (Microstructure profiler data), and at Kadko (2021) via https://doi.org/10.26008/1912/bco-dmo.861596.1 ($^{7}$Be measurements).

**Acknowledgments**
The method comparison presented in this paper was initiated by Dr. David Kadko. Sadly, he passed away in February 2022. The authors dedicate this paper to David's memory. This work was supported by NSF grant OPP-1753423 to DK and MS, and financial support for KS was available through the German (BMBF) and UK (NERC) funded PEANUTS-project (Grant 03F0804A). IF received funding through the AROMA (Arctic Ocean mixing processes and vertical fluxes of energy and matter) project by the Research Council of Norway, Grant 294396. Data used in this manuscript were produced as part of the international Multidisciplinary drifting Observatory for the Study of the Arctic Climate (MOSAiC) project with the tag MOSAiC20192020 and the Project_ID: AWI_PS122_00. We thank all persons involved in the expedition of the Research Vessel Polarstern during MOSAiC in 2019-2020 as listed in the MOSAiC extended acknowledgement (Nixdorf et al., 2021), and in particular Chris Marsay, Patric Simoes Pereira, Adela Dumitrascu, and all "ocean friends" contributing to the microstructure measurements. We would also like to thank two reviewers for providing detailed and helpful comments. Open Access funding enabled and organized by Projekt DEAL.

## References

Aaboe, E., Dion, E. P., & Turekian, K. K. (1981). 7Be in Sargasso Sea and long Island sound waters. *Journal of Geophysical Research: Oceans*, *86*(C4), 3255–3257. https://doi.org/10.1029/JC086iC04p03255

Ardyna, M., Babin, M., Gosselin, M., Devred, E., Rainville, L., & Tremblay, J.-É. (2014). Recent Arctic Ocean sea ice loss triggers novel fall phytoplankton blooms. *Geophysical Research Letters*, *41*(17), 6207–6212. https://doi.org/10.1002/2014GL061047

Babin, M. (2020). Climate change tweaks Arctic marine ecosystems. *Science*, *369*(6500), 137–138. https://doi.org/10.1126/science.abd1231

Baker, M. A., & Gibson, C. H. (1987). Sampling turbulence in the stratified ocean: Statistical consequences of strong intermittency. *Journal of Physical Oceanography*, *17*(10), 1817–1836. https://doi.org/10.1175/1520-0485(1987)017<1817:stitso>2.0.co;2

Bouffard, D., & Boegman, L. (2013). A diapycnal diffusivity model for stratified environmental flows. *Dynamics of Atmospheres and Oceans*, *61*, 14–34. https://doi.org/10.1016/j.dynatmoce.2013.02.002

Bourgain, P., & Gascard, J.-C. (2011). The Arctic Ocean halocline and its interannual variability from 1997 to 2008. *Deep Sea Research Part I: Oceanographic Research Papers*, *58*(7), 745–756. https://doi.org/10.1016/j.dsr.2011.05.001

Cael, B., & Mashayek, A. (2021). Log-skew-normality of ocean turbulence. *Physical Review Letters*, *126*(22), 224502. https://doi.org/10.1103/PhysRevLett.126.224502

Cámara-Mor, P., Masque, P., Garcia-Orellana, J., Kern, S., Cochran, J., & Hanfland, C. (2011). Interception of atmospheric fluxes by Arctic sea ice: Evidence from cosmogenic 7Be. *Journal of Geophysical Research: Oceans*, *116*(C12), C12041. https://doi.org/10.1029/2010JC006847

Carmack, E., Polyakov, I., Padman, L., Fer, I., Hunke, E., Hutchings, J., et al. (2015). Toward quantifying the increasing role of oceanic heat in sea ice loss in the new Arctic. *Bulletin of the American Meteorological Society*, *96*(12), 2079–2105. https://doi.org/10.1175/BAMS-D-13-00177.1

Dosser, H., Chanona, M., Waterman, S., Shibley, N., & Timmermans, M.-L. (2021). Changes in internal wave-driven mixing across the Arctic Ocean: Finescale estimates from an 18-year pan-Arctic record. *Geophysical Research Letters*, *48*(8), e2020GL091747. https://doi.org/10.1029/2020GL091747

Fer, I. (2009). Weak vertical diffusion allows maintenance of cold halocline in the central Arctic. *Atmospheric and Oceanic Science Letters*, *2*(3), 148–152. https://doi.org/10.1080/16742834.2009.11446789

Fer, I., Koenig, Z., Kozlov, I. E., Ostrowski, M., Rippeth, T. P., Padman, L., et al. (2020). Tidally forced lee waves drive turbulent mixing along the Arctic Ocean margins. *Geophysical Research Letters*, *47*(16), e2020GL088083. https://doi.org/10.1029/2020GL088083

Fine, E. C., & Cole, S. T. (2022). Decadal observations of internal wave energy, shear, and mixing in the Western Arctic Ocean. *Journal of Geophysical Research: Oceans*, *127*(5), e2021JC018056. https://doi.org/10.1029/2021JC018056

Gregg, M., D'Asaro, E., Riley, J., & Kunze, E. (2018). Mixing efficiency in the ocean. *Annual Review of Marine Science*, *10*(1), 443–473. https://doi.org/10.1146/annurev-marine-121916-063643

Haskell, W. Z., II, Kadko, D., Hammond, D. E., Knapp, A. N., Prokopenko, M. G., Berelson, W. M., & Capone, D. G. (2015). Upwelling velocity and eddy diffusivity from 7Be measurements used to compare vertical nutrient flux to export POC flux in the Eastern Tropical South Pacific. *Marine Chemistry*, *168*, 140–150. https://doi.org/10.1016/j.marchem.2014.10.004

Holtermann, P. L., Umlauf, L., Tanhua, T., Schmale, O., Rehder, G., & Waniek, J. J. (2012a). The Baltic Sea tracer release experiment: 1. Mixing rates. *Journal of Geophysical Research: Oceans*, *117*(C1). https://doi.org/10.1029/2011JC007445

Holtermann, P. L., Umlauf, L., Tanhua, T., Schmale, O., Rehder, G., & Waniek, J. J. (2012b). The Baltic Sea tracer release experiment: 2. Mixing processes. *Journal of Geophysical Research: Oceans*, *117*(C1). https://doi.org/10.1029/2011JC007439

Hsieh, Y.-T., Geibert, W., Woodward, E. M. S., Wyatt, N. J., Lohan, M. C., Achterberg, E. P., & Henderson, G. M. (2021). Radium-228-derived ocean mixing and trace element inputs in the South Atlantic. *Biogeosciences*, *18*(5), 1645–1671. https://doi.org/10.5194/bg-18-1645-2021

Kadko, D. (2000). Modeling the evolution of the Arctic mixed layer during the fall 1997 surface heat budget of the Arctic Ocean (SHEBA) project using measurements of 7be. *Journal of Geophysical Research: Oceans*, *105*(C2), 3369–3378. https://doi.org/10.1029/1999JC900311

Kadko, D. (2009). Rapid oxygen utilization in the ocean twilight zone assessed with the cosmogenic isotope 7be. *Global Biogeochemical Cycles*, *23*(4). https://doi.org/10.1029/2009GB003510

Kadko, D. (2021). Water column Beryllium-7 from samples collected on the MOSAiC expedition, PS122, on R/V Polarstern in the Central Arctic Ocean during 2019-2020 [Dataset]. Biological and Chemical Oceanography Data Management Office (BCO-DMO). https://doi.org/10.26008/1912/bco-dmo.861596.1

Kadko, D., Aguilar-Islas, A., Bolt, C., Buck, C. S., Fitzsimmons, J. N., Jensen, L. T., et al. (2019). The residence times of trace elements determined in the surface Arctic Ocean during the 2015 US Arctic GEOTRACES expedition. *Marine Chemistry*, *208*, 56–69. https://doi.org/10.1016/j.marchem.2018.10.011

Kadko, D., Aguilar-Islas, A., Buck, C. S., Fitzsimmons, J. N., Landing, W. M., Shiller, A., et al. (2020). Sources, fluxes and residence times of trace elements measured during the US GEOTRACES East Pacific Zonal Transect. *Marine Chemistry*, *222*, 103781. https://doi.org/10.1016/j.marchem.2020.103781

Kadko, D., Galfond, B., Landing, W. M., & Shelley, R. U. (2016). Determining the pathways, fate, and flux of atmospherically derived trace elements in the Arctic Ocean/ice system. *Marine Chemistry*, *182*, 38–50. https://doi.org/10.1016/j.marchem.2016.04.006

Kadko, D., & Johns, W. (2011). Inferring upwelling rates in the equatorial Atlantic using 7Be measurements in the upper ocean. *Deep Sea Research Part I: Oceanographic Research Papers*, *58*(6), 647–657. https://doi.org/10.1016/j.dsr.2011.03.004

Kadko, D., & Olson, D. (1996). Beryllium-7 as a tracer of surface water subduction and mixed-layer history. *Deep Sea Research Part I: Oceanographic Research Papers*, *43*(2), 89–116. https://doi.org/10.1016/0967-0637(96)00011-8

Kadko, D., & Swart, P. (2004). The source of the high heat and freshwater content of the upper ocean at the SHEBA site in the Beaufort Sea in 1997. *Journal of Geophysical Research: Oceans*, *109*(C1), C01022. https://doi.org/10.1029/2002JC001734

Krishnaswami, S., Lal, D., Somayajulu, B., Dixon, F., Stonecipher, S., & Craig, H. (1972). Silicon, radium, thorium, and lead in seawater: In-situ extraction by synthetic fibre. *Earth and Planetary Science Letters*, *16*(1), 84–90. https://doi.org/10.1016/0012-821X(72)90240-3

Krumpen, T., von Albedyll, L., Goessling, H. F., Hendricks, S., Juhls, B., Spreen, G., et al. (2021). Mosaic drift expedition from October 2019 to July 2020: Sea ice conditions from space and comparison with previous years. *The Cryosphere*, *15*(8), 3897–3920. https://doi.org/10.5194/tc-15-3897-2021

Lal, D., Chung, Y., Platt, T., & Lee, T. (1988). Twin cosmogenic radiotracer studies of phosphorus recycling and chemical fluxes in the upper ocean. *Limnology & Oceanography*, *33*(6), 1559–1567. https://doi.org/10.4319/lo.1988.33.6part2.1559

Ledwell, J. R., McGillicuddy, D. J., Jr., & Anderson, L. A. (2008). Nutrient flux into an intense deep chlorophyll layer in a mode-water eddy. *Deep Sea Research Part II: Topical Studies in Oceanography*, *55*(10–13), 1139–1160. https://doi.org/10.1016/j.dsr2.2008.02.005

Ledwell, J. R., St. Laurent, L. C., Girton, J. B., & Toole, J. M. (2011). Diapycnal mixing in the Antarctic circumpolar current. *Journal of Physical Oceanography*, *41*(1), 241–246. https://doi.org/10.1175/2010JPO4557.1

Ledwell, J. R., Watson, A. J., & Law, C. S. (1998). Mixing of a tracer in the pycnocline. *Journal of Geophysical Research: Oceans*, *103*(C10), 21499–21529. https://doi.org/10.1029/98JC01738

Lee, T., Barg, E., & Lal, D. (1991). Studies of vertical mixing in the Southern California Bight with cosmogenic radionuclides 32P and 7Be. *Limnology & Oceanography*, *36*(5), 1044–1052. https://doi.org/10.4319/lo.1991.36.5.1044

Lenn, Y.-D., Wiles, P., Torres-Valdes, S., Abrahamsen, E., Rippeth, T., Simpson, J., et al. (2009). Vertical mixing at intermediate depths in the Arctic boundary current. *Geophysical Research Letters*, *36*(5), L05601. https://doi.org/10.1029/2008GL036792

Lewis, M. R., Hebert, D., Harrison, W. G., Platt, T., & Oakey, N. S. (1986). Vertical nitrate fluxes in the oligotrophic ocean. *Science*, *234*(4778), 870–873. https://doi.org/10.1126/science.234.4778.870

McDougall, T. J., & Barker, P. M. (2011). Getting started with TEOS-10 and the Gibbs Seawater (GSW) oceanographic toolbox. *SCOR/IAPSO WG*, *127*, 1–28.

Meyer, A., Fer, I., Sundfjord, A., & Peterson, A. K. (2017). Mixing rates and vertical heat fluxes north of Svalbard from Arctic winter to spring. *Journal of Geophysical Research: Oceans*, *122*(6), 4569–4586. https://doi.org/10.1002/2016JC012441

Nixdorf, U., Dethloff, K., Rex, M., Shupe, M., Sommerfeld, A., Perovich, D. K., et al. (2021). Mosaic extended acknowledgement [Dataset]. Zenodo. https://doi.org/10.5281/zenodo.5541624

Osborn, T. (1980). Estimates of the local rate of vertical diffusion from dissipation measurements. *Journal of Physical Oceanography*, *10*(1), 83–89. https://doi.org/10.1175/1520-0485(1980)010⟨0083:EOTLRO⟩2.0.CO;2

Oschlies, A. (2002). Nutrient supply to the surface waters of the North Atlantic: A model study. *Journal of Geophysical Research: Oceans*, *107*(C5), 14–21. https://doi.org/10.1029/2000JC000275

Painter, S., Henson, S., Forryan, A., Steigenberger, S., Klar, J., Stinchcombe, M., et al. (2014). An assessment of the vertical diffusive flux of iron and other nutrients to the surface waters of the subpolar North Atlantic Ocean. *Biogeosciences*, *11*(8), 2113–2130. https://doi.org/10.5194/bg-11-2113-2014

Peterson, A. K., Fer, I., McPhee, M. G., & Randelhoff, A. (2017). Turbulent heat and momentum fluxes in the upper ocean under Arctic Sea ice. *Journal of Geophysical Research: Oceans*, *122*(2), 1439–1456. https://doi.org/10.1002/2016JC012283

Polyakov, I. V., Pnyushkov, A. V., Alkire, M. B., Ashik, I. M., Baumann, T. M., Carmack, E. C., et al. (2017). Greater role for Atlantic inflows on sea-ice loss in the eurasian basin of the Arctic Ocean. *Science*, *356*(6335), 285–291. https://doi.org/10.1126/science.aai8204

Polyakov, I. V., Rippeth, T. P., Fer, I., Alkire, M. B., Baumann, T. M., Carmack, E. C., et al. (2020). Weakening of cold halocline layer exposes sea ice to oceanic heat in the eastern Arctic Ocean. *Journal of Climate*, *33*(18), 8107–8123. https://doi.org/10.1175/JCLI-D-19-0976.1

Polyakov, I. V., Rippeth, T. P., Fer, I., Baumann, T. M., Carmack, E. C., & Ivanov, V. V., (2020b). Intensification of near-surface currents and shear in the eastern Arctic Ocean. *Geophysical Research Letters*, *47*(16), e2020GL089469. https://doi.org/10.1029/2020GL089469

Rabe, B., Heuzé, C., Regnery, J., Aksenov, Y., Allerholt, J., Athanase, M., et al. (2022). Overview of the MOSAiC expedition: Physical oceanography. *Elementa: Science of the Anthropocene*, *10*(1). https://doi.org/10.1525/elementa.2021.00062

Rainville, L., & Winsor, P. (2008). Mixing across the Arctic Ocean: Microstructure observations during the Beringia 2005 expedition. *Geophysical Research Letters*, *35*(8), L08606. https://doi.org/10.1029/2008GL033532

Randelhoff, A., Holding, J., Janout, M., Sejr, M. K., Babin, M., Tremblay, J.-E., & Alkire, M. B. (2020). Pan-arctic Ocean primary production constrained by turbulent nitrate fluxes. *Frontiers in Marine Science*, *7*, 150. https://doi.org/10.3389/fmars.2020.00150

Rippeth, T. P., & Fine, E. C. (2022). Turbulent mixing in a changing Arctic Ocean. *Oceanography*, *35*. https://doi.org/10.5670/oceanog.2022.103

Rippeth, T. P., Lincoln, B. J., Lenn, Y.-D., Green, J. M., Sundfjord, A., & Bacon, S. (2015). Tide-mediated warming of Arctic halocline by Atlantic heat fluxes over rough topography. *Nature Geoscience*, *8*(3), 191–194. https://doi.org/10.1038/ngeo2350

Schulz, K., Mohrholz, V., Fer, I., Janout, M. A., Hoppmann, M., Schaffer, J., et al. (2022). Turbulent microstructure profile (MSS) measurements from the MOSAiC drift, Arctic Ocean. [Dataset]. PANGAEA. https://doi.org/10.1594/PANGAEA.939816

Schulz, K., Büttner, S., Rogge, A., Janout, M., Hölemann, J., & Rippeth, T. P. (2021). Turbulent mixing and the formation of an intermediate nepheloid layer above the Siberian continental shelf break. *Geophysical Research Letters*, *48*(9), e2021GL092988. https://doi.org/10.1029/2021GL092988

Schulz, K., Janout, M., Lenn, Y.-D., Ruiz-Castillo, E., Polyakov, I., Mohrholz, V., et al. (2021). On the along-slope heat loss of the boundary current in the eastern Arctic Ocean. *Journal of Geophysical Research: Oceans*, *126*(2), e2020JC016375. https://doi.org/10.1029/2020JC016375

Schulz, K., Lincoln, B., Povazhnyy, V., Rippeth, T., Lenn, Y.-D., Janout, M., et al. (2022). Increasing nutrient fluxes and mixing regime changes in the eastern Arctic Ocean. *Geophysical Research Letters*, *49*(5), e2021GL096152. https://doi.org/10.1029/2021GL096152

Schulz, K., Mohrholz, V., Fer, I., Janout, M., Hoppmann, M., Schaffer, J., & Koenig, Z. (2022). A full year of turbulence measurements from a drift campaign in the Arctic Ocean 2019—2020. *Scientific Data*, *9*(472), 472. https://doi.org/10.1038/s41597-022-01574-1

Shaw, W. J., & Stanton, T. P. (2014). Vertical diffusivity of the Western Arctic Ocean halocline. *Journal of Geophysical Research: Oceans*, *119*(8), 5017–5038. https://doi.org/10.1002/2013JC009598

Silker, W. B. (1972). Beryllium-7 and fission products in the GEOSECS II water column and applications of their oceanic distributions. *Earth and Planetary Science Letters*, *16*(1), 131–137. https://doi.org/10.1016/0012-821X(72)90247-6

Sirevaag, A., & Fer, I. (2012). Vertical heat transfer in the Arctic Ocean: The role of double-diffusive mixing. *Journal of Geophysical Research: Oceans*, *117*(C7). https://doi.org/10.1029/2012JC007910

Stanton, T. P., Shaw, W. J., & Hutchings, J. K. (2012). Observational study of relationships between incoming radiation, open water fraction, and oceanocean-to-ice heat flux in the transpolar drift: 2002–2010. *Journal of Geophysical Research: Oceans*, *117*(C7). https://doi.org/10.1029/2011JC007871

Timmermans, M.-L., & Marshall, J. (2020). Understanding Arctic Ocean circulation: A review of ocean dynamics in a changing climate. *Journal of Geophysical Research: Oceans*, *125*(4), e2018JC014378. https://doi.org/10.1029/2018JC014378

Tremblay, J.-E., Anderson, L. G., Matrai, P., Coupel, P., Bélanger, S., Michel, C., & Reigstad, M. (2015). Global and regional drivers of nutrient supply, primary production and $CO_2$ drawdown in the changing Arctic Ocean. *Progress in Oceanography*, *139*, 171–196. https://doi.org/10.1016/j.pocean.2015.08.009

Vasholz, D. P., & Crawford, L. J. (1985). Dye dispersion in the seasonal thermocline. *Journal of Physical Oceanography*, *15*(6), 695–712. https://doi.org/10.1175/1520-0485(1985)015⟨0695:DDITST⟩2.0.CO;2

Wagener, T., Guieu, C., Losno, R., Bonnet, S., & Mahowald, N. (2008). Revisiting atmospheric dust export to the Southern Hemisphere ocean: Biogeochemical implications. *Global Biogeochemical Cycles*, *22*(2). https://doi.org/10.1029/2007GB002984

Young, J., & Silker, W. (1980). Aerosol deposition velocities on the Pacific and Atlantic oceans calculated from 7Be measurements. *Earth and Planetary Science Letters*, *50*(1), 92–104. https://doi.org/10.1016/0012-821X(80)90121-1